J. Fluid Mech. (2003), *vol.* 492, *pp.* 63–89.
DOI: 10.1017/S0022112003005469 Printed in the United Kingdom

Multiple states, stability and bifurcations of natural convection in a rectangular cavity with partially heated vertical walls

By V. ERENBURG[1], A. YU. GELFGAT[1], E. KIT[1], P. Z. BAR-YOSEPH[2] AND A. SOLAN[2]

[1]Department of Fluid Mechanics and Heat Transfer, Tel-Aviv University, Ramat Aviv 69978, Israel

[2]Computational Mechanics Laboratory, Faculty of Mechanical Engineering, Technion – Israel Institute of Technology, Haifa 32000, Israel

(Received 23 November 2001 and in revised form 25 April 2003)

The multiplicity, stability and bifurcations of low-Prandtl-number steady natural convection in a two-dimensional rectangular cavity with partially and symmetrically heated vertical walls are studied numerically. The problem represents a simple model of a set-up in which the height of the heating element is less than the height of the molten zone. The calculations are carried out by the global spectral Galerkin method. Linear stability analysis with respect to two-dimensional perturbations, a weakly nonlinear approximation of slightly supercritical states and the arclength path-continuation technique are implemented. The symmetry-breaking and Hopf bifurcations of the flow are studied for aspect ratio (height/length) varying from 1 to 6. It is found that, with increasing Grashof number, the flow undergoes a series of turning-point bifurcations. Folding of the solution branches leads to a multiplicity of steady (and, possibly, oscillatory) states that sometimes reaches more than a dozen distinct steady solutions. The stability of each branch is studied separately. Stability and bifurcation diagrams, patterns of steady and oscillatory flows, and patterns of the most dangerous perturbations are reported. Separated stable steady-state branches are found at certain values of the governing parameters. The appearance of the complicated multiplicity is explained by the development of the stably and unstably stratified regions, where the damping and the Rayleigh–Bénard instability mechanisms compete with the primary buoyancy force localized near the heated parts of the vertical boundaries. The study is carried out for a low-Prandtl-number fluid with $Pr = 0.021$. It is shown that the observed phenomena also occur at larger Prandtl numbers, which is illustrated for $Pr = 10$. Similar three-dimensional instabilities that occur in a cylinder with a partially heated sidewall are discussed.

1. Introduction

Various numerical and experimental studies of the stability of steady natural convective flows of a low-Prandtl-number fluid were motivated by crystal growth applications (Müller & Ostrogorsky 1994). A common computational model, among others, is the flow in cavities with uniformly and differentially heated sidewalls (see Gelfgat, Bar-Yoseph & Yarin 1997, 1999*a* and references therein). This model is associated with the horizontal Bridgman growth device. Other crystal growth set-ups (e.g. vertical Bridgman, floating zone) contain a vertical axisymmetric volume

of fluid heated at the vertical boundaries and cooled at the horizontal ones. This leads to problems of another type, where the instability of a primary axisymmetric flow leads to the development of a three-dimensional flow pattern. Examples of such instabilities are given in Gelfgat *et al.* (1999*b*, 2000). In all these models, the whole vertical boundary is heated either uniformly or non-uniformly. In practice, however, the size of a heater can be smaller than the vertical extent of the fluid volume, so that only a part of the vertical boundary is heated. It turns out that the convective flow caused by such local heating gives rise to an unexpectedly rich variety of flow patterns that can exist simultaneously. For example, it is shown here that at sufficiently large Grashof numbers, the initially symmetric steady-flow localized near the heated parts of the vertical boundary undergoes a transition, which localizes the most intensive motion rather far from the heated parts. In the present paper, we study the multiplicity and stability of possible steady-flow states using a simplified two-dimensional model.

A simple model (both experimental and computational) to study the instabilities of natural convection flow in a cylinder with a partially heated sidewall was considered by Selver, Kamotani & Ostrach (1998) in connection with floating-zone crystal growth. Convection in a vertical cylinder whose sidewall is heated in the middle and is thermally insulated above and below the heating zone was considered. As a simplified case, Selver *et al.* (1998) considered a flow in a rectangular cavity with piecewise heated and insulated vertical boundaries. Bifurcations of symmetry breaking and Hopf (oscillatory instability) were reported in that study for aspect ratios ($A = \text{height}/\text{length}$) 6 and 2, respectively.

The initial goal of the present work was to investigate the two bifurcations reported in Selver *et al.* (1998) for rectangular cavities with aspect ratio varying from 1 to 6 (figure 1) and the low Prandtl number $Pr = 0.021$ (the experimental liquid in Selver *et al.* (1998) was gallium), as a prelude to the three-dimensional cylindrical geometry. However, it was found that this particular and relatively simple model contains a variety of stable and unstable multiple steady and oscillatory states, so that beyond a certain value of the Grashof number (but below the threshold to turbulence) the final asymptotic flow state depends on particular initial conditions. In this paper, we present bifurcation and stability diagrams related to the multiple steady-flow states. We show also that the conclusions made for the two-dimensional case remain qualitatively similar for the three-dimensional instability of an axisymmetric flow corresponding to the experimental configuration of Selver *et al.* (1998). We show also that the observed phenomena are preserved qualitatively also for larger Prandtl numbers, which we illustrate for $Pr = 10$. We further argue that the observed multiplicity of flow states is expected to be a common phenomenon for other, practically important configurations where only a part of a vertical boundary is heated.

The existence of multiple flow states in confined flows was observed experimentally and numerically for convection in infinite layers and finite cavities heated from below (Busse 1967; Cross *et al.* 1983; Gelfgat 1999; Pallares, Grau & Giralt 1999) and from the side (Bergholz 1978; Tsitverblit & Kit 1993; Gelfgat *et al.* 1999*a*), Taylor–Couette configurations (Coles 1965; Cliffe & Mullin 1985), flow between rotating spheres (Schrauf 1986; Bar-Yoseph 1994) and other problems. As a rule, the multiplicity manifests itself as different numbers of vortices or rolls, one similar to another. In other cases, different flow patterns can be associated with different symmetries of a problem. In the configuration considered here, the developing multiple states transform from an initial symmetric pattern to multiple non-symmetric states, where the most intensive motion develops unexpectedly far from the heated parts of the boundaries (see figures 2 and 3 below). This transition, characteristic for tall

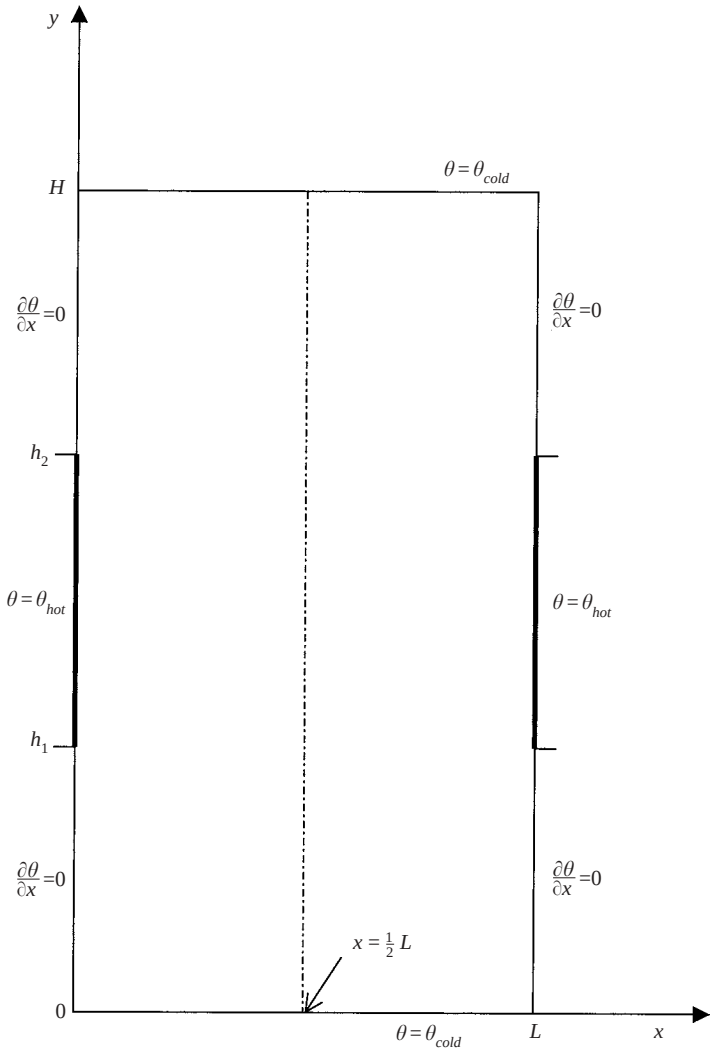

FIGURE 1. Geometry of the problem.

two- and three-dimensional cavities and existing in a wide range of Prandtl numbers, is revealed and explained in the present paper.

The problem sketched in figure 1 corresponds, roughly, to the configuration studied by Selver *et al.* (1998). In the present paper, it was solved numerically using the global Galerkin method with the basis functions proposed by Gelfgat & Tanasawa (1994). The whole computational approach, which includes the calculation of steady flows, analysis of their linear stability and weakly nonlinear asymptotic approximation of slightly supercritical states, is described in Gelfgat (2001). A newly developed extension implementing a discontinuous temperature boundary condition in a continuous Galerkin basis is described here.

In the course of the present investigation of the two-dimensional symmetry-breaking and Hopf bifurcations, it was found that at all the aspect ratios considered, the convective flows undergo a series of turning-point bifurcations. Folding of the steady-state branches leads to a multiplicity of steady states. Consequently, the stability of

each steady-state branch has to be studied separately. The number of distinct multiple steady states sometimes reaches thirteen (e.g. at $A = 2$). Although most of the multiple states are found to be unstable, there exist also stable steady branches (at least with respect to the two-dimensional perturbations) which can be reached numerically only with the use of an appropriate path-continuation technique. The detailed parametric study allows us to find steady-state branches separated from other solutions. It is assumed that distinct unstable steady flows can trigger the appearance of distinct oscillatory states, making the final stable asymptotic state strongly dependent on the particular initial conditions and the computational path. This can lead to a situation where the final oscillatory state of the flow is unpredictable while the flow regime is below the threshold to turbulence.

The variety and complexity of the turning-point bifurcations observed here seems to be a rare phenomenon for natural convection, as well as for other incompressible flows. These turning-point bifurcations are observed after the symmetry breaking instability sets in. It is shown that the multiplicity is caused by the combined action of the buoyancy force located near the heated parts of vertical boundaries, the Rayleigh–Bénard instability mechanisms inside the unstably stratified part of the flow, and flow damping inside the stably stratified part.

Most of the results reported here are obtained for the two-dimensional flow model (figure 1) whose stability is examined with respect to two-dimensional perturbations. The question is how can the conclusions made here be applied to a realistic three-dimensional case? To answer this question three different three-dimensional models can be considered: (i) a two-dimensional basic state with three-dimensional perturbations periodic in the third dimension; (ii) a three-dimensional box with no-slip boundaries and fully three-dimensional base state and perturbations; and (iii) a vertical cylinder with a partially and axisymmetrically heated sidewall, assuming an axisymmetric base state and three-dimensional perturbations two-periodic in the circumferential direction. Consideration of model (i) will lead to the same multiple two-dimensional steady states as in the wholly two-dimensional model treated here, but some of them, stable within the two-dimensional model, will be unstable with respect to three-dimensional perturbations with a certain spatial period. Such a study would require a series of runs each time the critical spatial period has to be found, leading to an unaffordable amount of computation. Furthermore, it would not provide the answer regarding a simple three-dimensional box. Model (ii) can be considered by the three-dimensional version of our numerical technique described in Gelfgat (1999). In this case, an additional governing parameter is the width ratio of the cavity (width/length), which will strongly affect both the base flows and their stability properties. A computational simulation of this model could be justified if there existed an experiment for which the value of the width ratio was defined. In fact, the experiment of Selver *et al.* (1998) which motivated our study was performed in cylindrical geometry, which leads us to the choice of model (iii). Considering this model, we reveal several similarities of the symmetry-breaking transitions in the two-dimensional plane model and the axisymmetry – three-dimensional transition in a finite vertical cylinder.

Note that natural convection in enclosures with partially heated boundaries is usually motivated by heat transfer engineering problems, e.g. the cooling of electronic devices, solar energy collection, nuclear reactor operation, and safety and energy efficient design of buildings, rooms and machinery (Kitamura, Komiyama & Saito 1984; Poulikakos 1985; Kalilollahi & Sammakia 1986; Kuhn & Oosthuizen 1987; November & Nansteel 1987; Keyhani, Prasad & Cox 1988; Chadwick, Webb &

Heaton 1991; Fu, Tseng & Chen 1994; Ho & Chang 1994; Lakhal *et al.* 1994, 1999; Sezai & Mohamad 2000; Frederick & Quiroz 2001). Most of these studies were focused on the heat transfer characteristics and considered convection of air or water whose Prandtl number Pr is about 0.7 and 7.0, respectively. As mentioned, the present study is mainly focused on a different class of problems, i.e. on the transitions in low-Prandtl-number fluid convection, of interest in connection with the uniformity of growing crystals. We show, however, that the Rayleigh–Bénard mechanism leads to a similar flow multiplicity also in such fluids as air and water, which would be significant also in heat transfer applications.

In the following, we describe characteristic stable and unstable flow patterns, several most characteristic bifurcation diagrams, the stability diagram of the flow, the most dangerous perturbations and the patterns of supercritical oscillatory flows. The paper is organized as follows. Section 2 contains the formulation of the problem. Some relevant details of the computational methods involved are presented in § 3. Results and a discussion are presented in § 4 and conclusions are drawn in § 5.

2. Formulation of the problem

Consider the convective flow of a Boussinesq fluid in a two-dimensional rectangular cavity $0 \leqslant x \leqslant L$, $0 \leqslant y \leqslant H$ (figure 1). All the boundaries are no-slip. The horizontal boundaries are maintained at a constant low temperature θ_{cold}. Parts of the vertical boundaries in the interval $h_1 \leqslant y \leqslant h_2$ are maintained at a high temperature θ_{hot}. The remaining parts of the vertical boundaries are thermally insulated.

To render the problem dimensionless, we introduce the scales L, L^2/ν, ν/L, $\rho(\nu/L)^2$ for length, time, velocity and pressure, respectively, where ν is the kinematic viscosity and ρ is the density. The temperature is rescaled as $\theta \rightarrow (\theta - \theta_{cold})/(\theta_{hot} - \theta_{cold})$. Then the set of Boussinesq equations for the non-dimensional velocity $\boldsymbol{v} = \{v_x, v_y\}$, temperature θ and pressure p reads

$$\frac{\partial \boldsymbol{v}}{\partial t} + (\boldsymbol{v} \cdot \nabla)\boldsymbol{v} = -\nabla p + \Delta \boldsymbol{v} + Gr\,\theta\,\boldsymbol{e}_y \tag{1}$$

$$\frac{\partial \theta}{\partial t} + (\boldsymbol{v} \cdot \nabla)\theta = \frac{1}{Pr}\Delta\theta, \tag{2}$$

$$\nabla \cdot \boldsymbol{v} = 0. \tag{3}$$

The boundary conditions are:

$$\boldsymbol{v} = \boldsymbol{0} \quad \text{on all the boundaries,} \tag{4}$$

$$\theta = 0 \quad \text{at} \quad y = 0, A, \tag{5}$$

$$\theta = 1 \quad \text{at} \quad x = 0, 1; \quad a_1 \leqslant y \leqslant a_2, \tag{6}$$

$$\frac{\partial \theta}{\partial x} = 0 \quad \text{at} \quad x = 0, 1; \quad y < a_1 \quad \text{or} \quad y > a_2. \tag{7}$$

Here, $Gr = g\beta(\theta_{hot} - \theta_{cold})L^3/\nu^2$ is the Grashof number, $Pr = \nu/\chi$ the Prandtl number, $A = H/L$ the aspect ratio of the cavity, $a_1 = h_1/L$ and $a_2 = h_2/L$ are the dimensionless borders of the heated regions, g is the acceleration due to gravity, β the thermal expansion coefficient, χ the thermal diffusivity, and $\boldsymbol{e}_y$ the unit vector in the vertical direction. Note that although the geometry and boundary conditions are symmetric with respect to the line $x = 0.5$, we consider the problem in the whole region, thus allowing for possible symmetry-breaking bifurcations. Since we are interested mainly in steady solutions of (1)–(7) and their stability, the initial conditions are not specified.

As was concluded in Gelfgat *et al.* (1997, 1999), the stability properties of a convective flow are strongly dependent on the geometric characteristic parameters and the Prandtl number, so that an extrapolation from a given value to close values is not always possible. It was further concluded that a computational modelling of a given experiment should be done for the same values of the characteristic parameters. Therefore, in the following, the values of Pr, a_1, and a_2 are not varied and are chosen to be $Pr = 0.021$, $a_1 = A/2 - 1/4$, $a_2 = A/2 + 1/4$, which are exactly the values of the experiment of Selver *et al.* (1998). The parametric study is performed in the parameter space of the Grashof number and the aspect ratio. We show further that the conclusions drawn for a small-Prandtl-number fluid remain qualitatively similar for the case of $Pr = 10$.

3. Computational method

Following our previous studies (Gelfgat & Tanasawa 1994; Gelfgat *et al.* 1996, 1997, 1999*a*, *b*; Gelfgat 1999, 2001) we use the global Galerkin method for the computation of steady states, analysis of their stability and weakly nonlinear approximation of slightly supercritical oscillatory states. The basis functions of the Galerkin method are constructed as linear superpositions of Chebyshev polynomials and satisfy the continuity equation (3) and the boundary conditions analytically (for details see Gelfgat & Tanasawa 1994; Gelfgat 2001). The main advantage of this approach is the relatively low dimension of the resulting dynamical system, which contains the Galerkin projections of the momentum and energy equations without any additional algebraic constraints. However, the polynomial basis functions cannot satisfy the boundary conditions (6) and (7), since owing to these conditions the derivatives $\partial\theta/\partial x$ and $\partial\theta/\partial y$ are discontinuous at the points $y = a_1$ and $y = a_2$ of the vertical boundaries. A change of the variables, such as was used in Gelfgat *et al.* (1996, 1999*b*) to account for the discontinuities of boundary conditions in the corners of flow regions, is not applicable in the present case. The computational approach was extended here to account for discontinuity points located inside a boundary. This extension is briefly described below.

The temperature is split into two functions as

$$\theta(x, y, t) = \Theta(x, y, t) + \tilde{\theta}(x, y, t), \tag{8}$$

where $\tilde{\theta}(x, y, t)$ is the new unknown function for which a continuous set of boundary conditions is required, i.e.

$$\tilde{\theta} = 0 \quad \text{at} \quad y = 0, A, \quad \frac{\partial\tilde{\theta}}{\partial x} = 0 \quad \text{at} \quad x = 0, 1. \tag{9}$$

The function $\Theta(x, y, t)$ is used to adjust the boundary conditions for $\theta(x, y)$ to (5)–(7). Therefore, the boundary conditions for $\Theta(x, y)$ are

$$\Theta = 0 \quad \text{at} \quad y = 0, A, \tag{10}$$

$$\Theta = 1 - \tilde{\theta} \quad \text{at} \quad x = 0, 1; \quad a_1 \leqslant y \leqslant a_2, \tag{11}$$

$$\frac{\partial\Theta}{\partial x} = 0 \quad \text{at} \quad x = 0, 1; \quad y < a_1 \quad \text{or} \quad y > a_2. \tag{12}$$

To avoid the appearance of an additional source term in the energy equation we also require that $\Theta(x, y, t)$ be a harmonic function:

$$\Delta\Theta = 0. \tag{13}$$

The solution of problem (10)–(13) can be represented as

$$\Theta(x, y, t) = \Theta_0(x, y) + \Theta_1(x, y, t), \tag{14}$$

where $\Theta_0(x, y)$ is the part of the solution of (10)–(13) corresponding to $\tilde{\theta} = 0$ and $\Theta_1(x, y, t)$ is the part dependent on $\tilde{\theta}$. Obviously, the part $\Theta_0(x, y)$ is defined by the geometry of the problem only. The problem for $\Theta_1(x, y, t)$ is defined as

$$\Delta\Theta_1 = 0, \tag{15a}$$

$$\Theta_1 = 0 \quad \text{at} \quad y = 0, A, \tag{15b}$$

$$\Theta_1 = -\tilde{\theta} \quad \text{at} \quad x = 0, 1; \quad a_1 \leqslant y \leqslant a_2, \tag{15c}$$

$$\frac{\partial\Theta_1}{\partial x} = 0 \quad \text{at} \quad x = 0, 1; \quad y < a_1 \quad \text{or} \quad y > a_2. \tag{15d}$$

Problem (15) can be represented in operator form as $\mathbf{Q}\Theta_1 = \mathbf{L}\tilde{\theta}$ and its solution as $\Theta_1 = \mathbf{T}\tilde{\theta}$, where $\mathbf{T} = \mathbf{Q}^{-1}\mathbf{L}$. The representation of the temperature, (8), now reads

$$\theta(x, y, t) = \Theta(x, y, t) + \tilde{\theta}(x, y, t) = \Theta_0(x, y, t) + (\mathbf{T} + \mathbf{I})\tilde{\theta}(x, y, t), \tag{16}$$

where $\mathbf{I}$ is the identity operator. Substitution of (16) into the energy equation (2) yields

$$(\mathbf{T} + \mathbf{I})\frac{\partial\tilde{\theta}}{\partial t} + (\boldsymbol{v}\cdot\nabla)(\mathbf{T} + \mathbf{I})\tilde{\theta} = \frac{1}{Pr}\Delta(\mathbf{T} + \mathbf{I})\tilde{\theta} - (\boldsymbol{v}\cdot\nabla)\Theta_0. \tag{17}$$

Thus, after the function Θ_0 and the operator $\mathbf{T}$ are obtained, the remaining unknown function is $\tilde{\theta}$, for which the boundary conditions are continuous and homogeneous. Now, the velocity $\boldsymbol{v}$ and the function $\tilde{\theta}$ are approximated by the series

$$\boldsymbol{v} = \sum_{i=1}^{N_x}\sum_{j=1}^{N_y} c_{ij}(t)\,\boldsymbol{u}_{ij}(x, y), \quad \tilde{\theta} = \sum_{i=1}^{M_x}\sum_{j=1}^{M_y} d_{ij}(t) q_{ij}(x, y), \tag{18}$$

where $c_{ij}(t)$ and $d_{ij}(t)$ are unknown time-dependent coefficients, and $\boldsymbol{u}_{ij}(x, y)$ and $q_{ij}(x, y)$ are the basis functions defined in Gelfgat & Tanasawa (1994). Additional details on the implementation of the global Galerkin method can be found in Gelfgat (2001).

After all the Galerkin projections are computed, and the function $\Theta_0(x, y)$ and the operator $\mathbf{T}$ are approximated with sufficient accuracy, the resulting dynamical system for the computation of the time-dependent coefficients $c_{ij}(t)$ and $d_{ij}(t)$ is obtained in the form:

$$\dot{X}_k(t) = L_{km}X_m(t) + N_{kml}X_m(t)X_l(t) + F_k, \tag{19}$$

where the vector $\boldsymbol{X}(t)$ contains all the coefficients $c_{ij}(t)$ and $d_{ij}(t)$, and the matrices $\mathbf{L}$, $\mathbf{N}$ and $\mathbf{F}$ are the Galerkin projections of linear and bilinear operators and free terms of (1) and (17), respectively. Note, that at this stage all the boundary conditions are satisfied and the pressure is excluded by projection on the divergence-free basis. Therefore, the dynamical system (19) does not contain any algebraic constraints. The steady solutions of (19) are computed by Newton iteration. The arclength continuation technique (Keller 1977) is applied where necessary. The linear stability of the computed steady states and weakly nonlinear approximation of the slightly supercritical oscillatory states are evaluated as described in Gelfgat (2001).

To compute the function $\Theta_0(x, y)$ and the approximation of the operator $\mathbf{T}$, the same Galerkin approach is applied to the problem (10)–(13). The basis functions used for the approximation of Θ and Θ_0 satisfy analytically the boundary condition (10).

The equations for the Galerkin coefficients are obtained by Galerkin projections of the Laplace equation (13) and Chebyshev collocations at the boundaries $x = 0$ and 1. After the Galerkin projections are applied, the operator $\mathbf{T}$ is approximated by a matrix. It was found that for the case $a_1 = A/2 - 1/4$, $a_2 = A/2 + 1/4$ that corresponds to that studied by Selver *et al.* (1998) and is considered below, 50 collocation points provide a sufficiently good approximation of the boundary conditions (11), (12), yielding a deviation of less than 1% from an independent numerical solution obtained by the finite-volume method on the uniform grid 100×100.

The test calculations were carried out to study the convergence of steady solutions and critical parameters corresponding to the transition from steady to oscillatory flow states. It was found that for aspect ratio in the range $1 \leqslant A \leqslant 6$ the use of 20×50 basis functions in the x- and y-directions, respectively, provides at least three converged decimal digits of the critical parameters. Comparison of the computed steady states with the independent finite-volume solution also shows that the deviation between the two solutions is seen only in the third or fourth decimal digit.

4. Results

Most of the computations were carried out for a fixed value of the Prandtl number, $Pr = 0.021$, and fixed position and length of the heated part of the lateral walls, $a_1 = A/2 - 1/4$, $a_2 = A/2 + 1/4$, i.e. the heated region is located in the middle of the sidewall and its dimensionless length is 0.5, corresponding to the experiment and calculation in Selver *et al.* (1998). The aspect ratio was varied in the range $1 \leqslant A \leqslant 6$. At each A, the Grashof number was varied so as to identify all relevant flow patterns. The linear stability with respect to two-dimensional perturbations only was examined for all the flow patterns obtained. As we explained above, the consideration of three-dimensional perturbations periodic in the third direction could reveal additional instabilities, but would not describe the behaviour of fully three-dimensional flow in a finite three-dimensional box. The three-dimensional instability of a similar axisymmetric flow in a vertical cylinder, corresponding to the experiments of Selver *et al.* (1998), is discussed in § 4.4.

Examples of the most characteristic flow patterns are shown in figure 2. More flow patterns are shown as inserts in the bifurcation diagrams (see below). At low Grashof numbers, the flow pattern is reflection symmetric consisting of two convective rolls, which rotate in opposite directions (figure 2*a*). With the increase of the Grashof number, the reflection symmetry of the flow can be broken, which takes place as either a Hopf or a steady bifurcation. In the first case (Hopf bifurcation) the supercritical flow consists of two non-symmetric oscillating vortices whose size increases and decreases during a period of oscillation. Such a transition from a steady symmetric to a non-symmetric oscillatory state was described in Selver *et al.* (1998). A snapshot of the streamlines of such flow is shown in figure 2(*b*). Another possibility, i.e. the break of symmetry via a steady bifurcation leads to a similar steady pattern. However, at larger Grashof numbers, this pattern changes drastically and transforms to that shown in figure 2(*c*). It is seen (figure 2*c*) that the flow can transform to a system of convective rolls placed one above another. In taller cavities, an additional roll (or rolls) appears above the two primary rolls, in the region where the fluid is unstably thermally stratified (see § 4.3). Obviously, because of the symmetry of the problem, for each non-symmetric flow pattern there exists its reflection-symmetric counterpart, which can be obtained by the transformation $x \to 1 - x$.

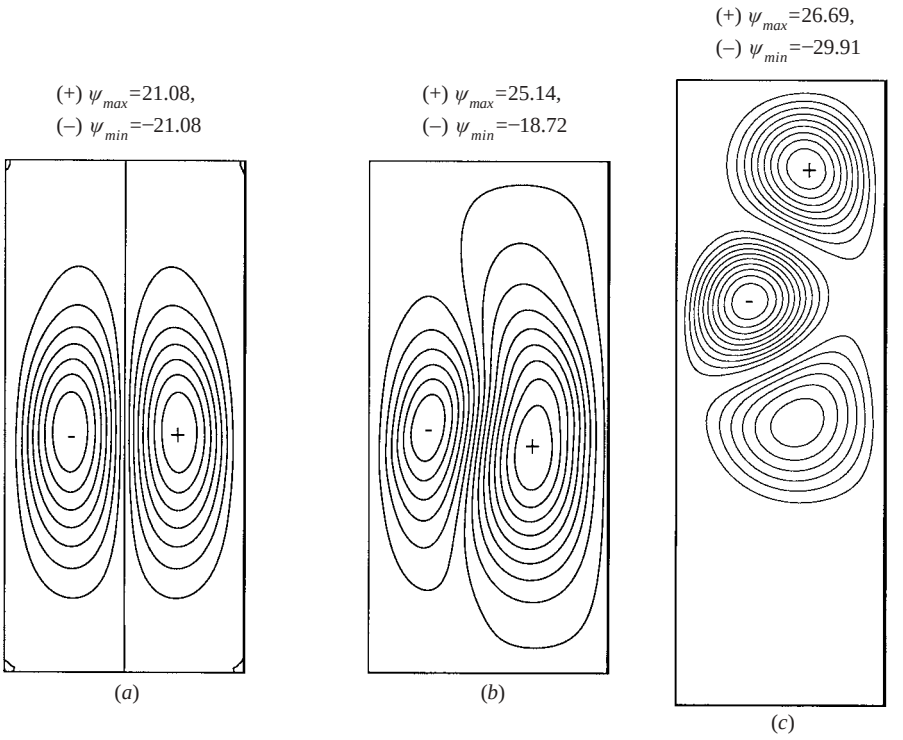

FIGURE 2. Examples of computed flow patterns. (*a*) Steady symmetric flow. $Gr = 1.4 \times 10^5$, $A = 2$. (*b*) Snapshot of non-symmetric oscillatory flow. $Gr = 1.5 \times 10^5$, $A = 2$. (*c*) Snapshot of non-symmetric oscillatory flow. $Gr = 5.71 \times 10^5$, $A = 2.8$.

To initiate the non-symmetric steady modes, an initial artificial asymmetry was introduced in the boundary conditions. Then the computed non-symmetric flow was used as an initial guess for the symmetric boundary conditions. Starting from a certain supercriticality (above the Grashof number corresponding to the steady symmetry-breaking bifurcation) the Newton iterations converged to a non-symmetric steady flow.

4.1. *An example of a bifurcation diagram*

To illustrate transitions between different steady-state branches, we define the Nusselt numbers at the hot parts of the left-hand and right-hand walls (figure 1) as

$$Nu_L = -\frac{1}{a_2 - a_1}\int_{a_1}^{a_2}\left[\frac{\partial\theta}{\partial x}\right]_{x=0} \mathrm{d}y, \quad Nu_R = \frac{1}{a_2 - a_1}\int_{a_1}^{a_2}\left[\frac{\partial\theta}{\partial x}\right]_{x=1} \mathrm{d}y, \tag{20}$$

and plot the difference $Nu_L - Nu_R$ versus the Grashof number. Obviously, for the symmetric states, the difference $Nu_L - Nu_R$ is zero. The non-zero values always correspond to non-symmetric states, which exhibit an unexpected multiplicity. In all bifurcation diagrams reported here and below, the stable flow branches are denoted by bold curves. Points corresponding to the primary symmetry-breaking and primary Hopf bifurcations are denoted as S and H, respectively. The turning points are denoted as T.

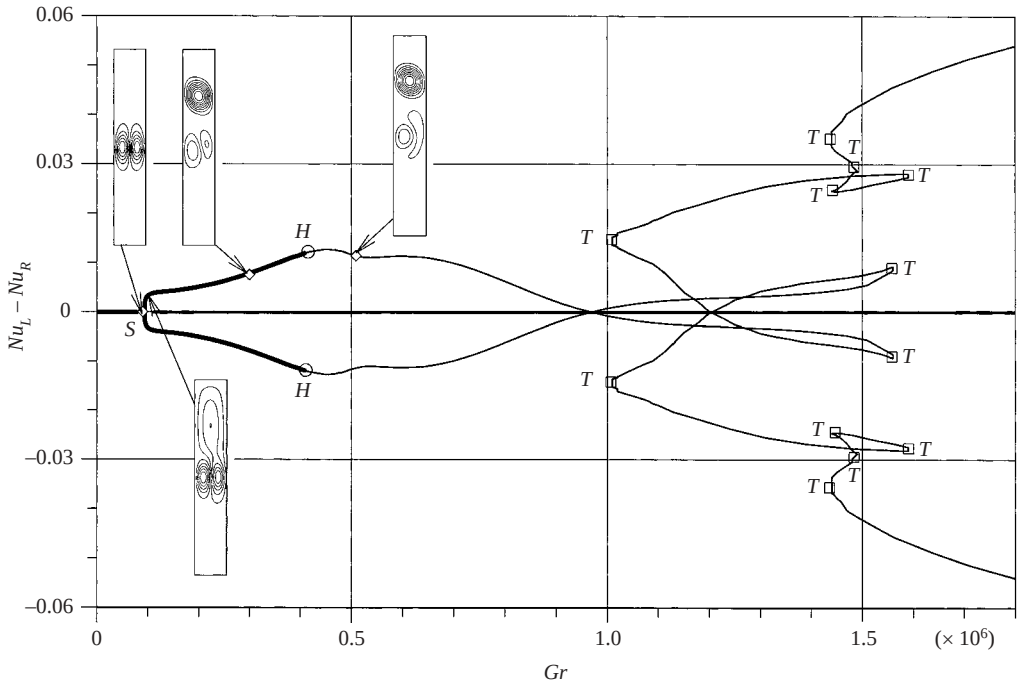

FIGURE 3. Bifurcation diagram for $A = 6.0$. Stable steady states are shown by bold lines. S, point of symmetry-breaking steady bifurcation; T, turning point; H, point of Hopf bifurcation. Symbols $\diamond$ correspond to the flow patterns shown as inserts.

Taking for example $A = 6$, the transitions of the flow patterns and changes in the difference $Nu_L - Nu_R$ with the increasing Grashof number are shown in figure 3. With the increase of the Grashof number from subcritical up to $Gr = 9.32 \times 10^4$ (point S) the flow remains symmetric, as illustrated by the corresponding insert. The steady symmetry-breaking bifurcation takes place at $Gr = 9.32 \times 10^4$ (point S). As a result, a non-symmetric flow pattern develops (see insert), which is indicated by a non-zero difference $Nu_L - Nu_R$. As seen from the example of the corresponding flow pattern (figure 3), the break of symmetry leads to a slight growth of one of the vortices and a slight decay of the other. With further increase of the Grashof number, the non-symmetric flow pattern continuously transforms, so that it consists of a primary vortex located in the upper part of the cavity and two weak vortices near the heated parts of the sidewall. Note, that this pattern is unexpected, since the flow near the heated parts of the boundaries weakens, while far from the heated parts the flow intensifies. The physical mechanisms leading to such a drastic change in the flow pattern are discussed below. This pattern persists until the flow becomes oscillatory-unstable. The Hopf bifurcation (oscillatory instability) takes place at $Gr = 4.09 \times 10^5$ (point H). At larger Grashof numbers, all steady states are oscillatory-unstable. However, following the development of unstable steady states with the increase of Gr, we find a complicated behaviour for $Gr > 10^6$ (figure 3). Thus, the unstable steady-state branch undergoes six turning-point bifurcations (at points T), so that 7 distinct steady states exist in the interval $1.01 \times 10^6 \leqslant Gr \leqslant 1.44 \times 10^6$ and even 13 states in the narrow interval $1.44 \times 10^6 \leqslant Gr \leqslant 1.49 \times 10^6$ which includes three turning points. As mentioned, all the steady states are oscillatory-unstable beyond the Hopf bifurcation point. Thus, around each unstable steady branch there exists a stable or unstable limit cycle,

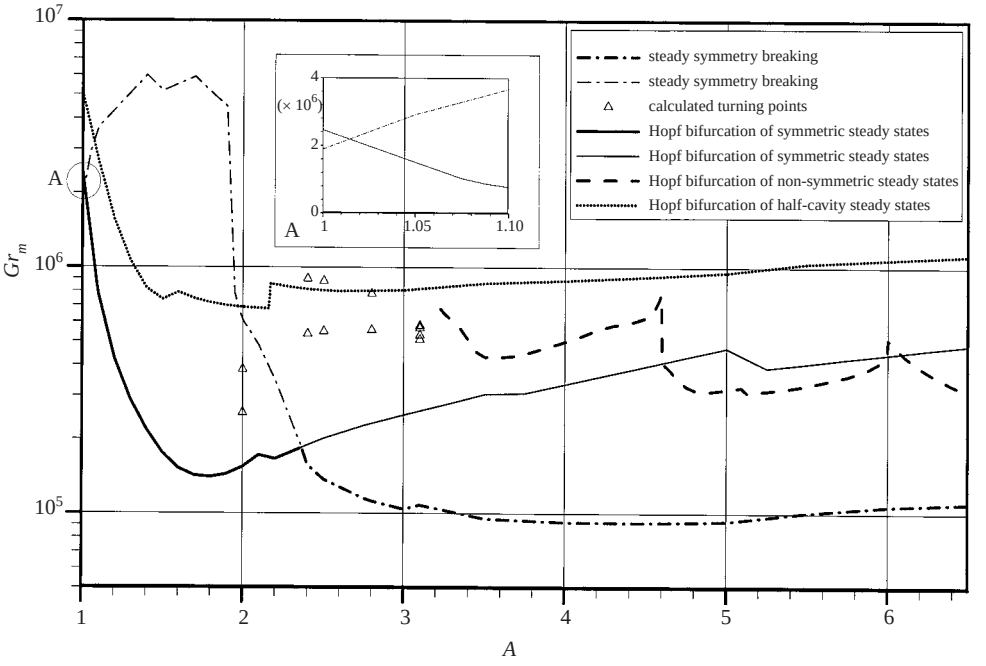

FIGURE 4. Stability diagram. Marginal values of the Grashof number versus the aspect ratio.

which means that a multiplicity of oscillatory flow states can be expected. We did not observe additional bifurcations of steady states up to $Gr = 10^7$. The stability diagrams for other values of the aspect ratio, as well as the physical mechanisms leading to the changes in the flow patterns, multiplicity and instability are discussed below.

4.2. *Stability diagram*

The primary goal of the present study is to describe the transitions between different steady and oscillatory flow states observed. The computed marginal stability curves, corresponding to the two-dimensional perturbations only, are shown in figure 4. The curves corresponding to the primary (steady or Hopf) and secondary (Hopf bifurcation of steady non-symmetric states) instabilities are shown in bold. The curves shown by thinner (non-bold) lines show the critical numbers of certain less dangerous modes. They were computed by neglecting the more dangerous modes, which means that the corresponding bifurcations cannot be observed either by a laboratory experiment, or by a straightforward integration in time.

At relatively small aspect ratios, in the interval $1.015 < A < 2.4$, the symmetric steady states become unstable via the symmetry-breaking Hopf bifurcation (solid line). For $1 \leqslant A \leqslant 1.015$ and $A > 2.4$, the symmetric steady states first become unstable owing to a steady symmetry-breaking pitchfork bifurcation (dash-and-dot curve) and transform into non-symmetric patterns similar to those shown as inserts in figure 3. At larger Grashof numbers, the non-symmetric steady flows become oscillatory owing to the Hopf bifurcation (dashed curve). We show also the marginal curve which was computed in half of the cavity, corresponding to $0 \leqslant x \leqslant 1/2$, with the symmetry conditions imposed at $x = 1/2$ (dotted curve). This corresponds to a study of stability of the symmetric steady states with respect to symmetric perturbations only. It follows that even though all boundary conditions of the problem are symmetric, consideration of the symmetric perturbations only (or the half-cavity problem) yields

overestimated critical Grashof numbers and obviously misses all possible symmetry-breaking bifurcations and non-symmetric solutions. In other words, the symmetric perturbation is not the most dangerous.

As was mentioned, parts of the marginal stability curves which cannot be observed experimentally or by a straightforward time-integration are shown by thinner lines. These curves, together with the dotted curve, indicate for which parameters a multiplicity of steady and oscillatory states can be expected. It will be shown below that above the marginal stability curves corresponding to the Hopf bifurcation (solid and dashed curves in figure 4) there can exist separated steady non-symmetric states, which can be stable or unstable depending on the characteristic parameters. In some cases, the steady–oscillatory transition takes place not due to the Hopf bifurcation, but as an abrupt jump to the unstable branch of steady solutions with the simultaneous development of finite-amplitude oscillations (see § 4.3). Such transitions were observed in the interval $2.4 < A < 3.2$, for which we could not compute a definite marginal curve separating the steady and oscillatory flow regimes. Several turning points, between which stable steady non-symmetric states were observed, are shown in figure 4.

The existence of the steady symmetry-breaking pitchfork bifurcation shows that a multiplicity of steady states should be expected beyond a certain value of the Grashof number (as shown in, e.g. figure 3). Thus, above the corresponding marginal stability curve (dash–dot line in figure 4) there exist at least one symmetric and one pair of non-symmetric steady states. As was mentioned, at the same values of A and Gr, the non-symmetric states, belonging to the same pair, can be transformed into each other by the transformation $x \to 1-x$. The stability properties of such a pair of steady states are identical, which is the consequence of the symmetry of the problem. At the same time, with the increase of the Grashof number, the first pair of non-symmetric steady states undergoes further turning-point bifurcations, such that the total number of the computed steady states sometimes reaches eleven (one symmetric and five pairs of non-symmetric states, see § 4.3) or even more. The results of the stability analysis show that, as a rule, among all multiple steady states there is either only one stable symmetric state, or only one stable pair of non-symmetric states, or all steady states are unstable. However, sometimes there exists a stable oscillatory state together with a stable steady state. Moreover, the instability of most of the unstable steady states occurs owing to a pair of complex conjugate eigenvalues, i.e. these states are oscillatory-unstable. Thus, limit cycles (oscillatory flow states) can be expected around each unstable stationary point (steady-state flow), which allows for a multiplicity of the supercritical oscillatory states. For example, above the dotted curve in figure 4, we usually expect to observe a non-symmetric oscillatory flow. However, there exists also a symmetric oscillatory state whose stability properties are unknown. The computation and stability analysis of possible multiple oscillatory flows are beyond the scope of present study.

4.3. *Bifurcation diagrams, flow and perturbation patterns*

In the following, we present bifurcation diagrams of steady-state flows for several characteristic aspect ratios and continuously varied Grashof number. As in figure 3, the stable branches of steady states are indicated in bold in all diagrams and the points corresponding to the primary symmetry-breaking and primary Hopf bifurcations are denoted as S and H, respectively. The turning points are denoted as T.

At $A = 1$ (figure 5), the symmetric steady flow loses its stability at $Gr = 1.80 \times 10^6$ (point S) and transforms into a non-symmetric steady flow via the steady symmetry-breaking pitchfork bifurcation. The patterns for non-symmetric steady flow and the

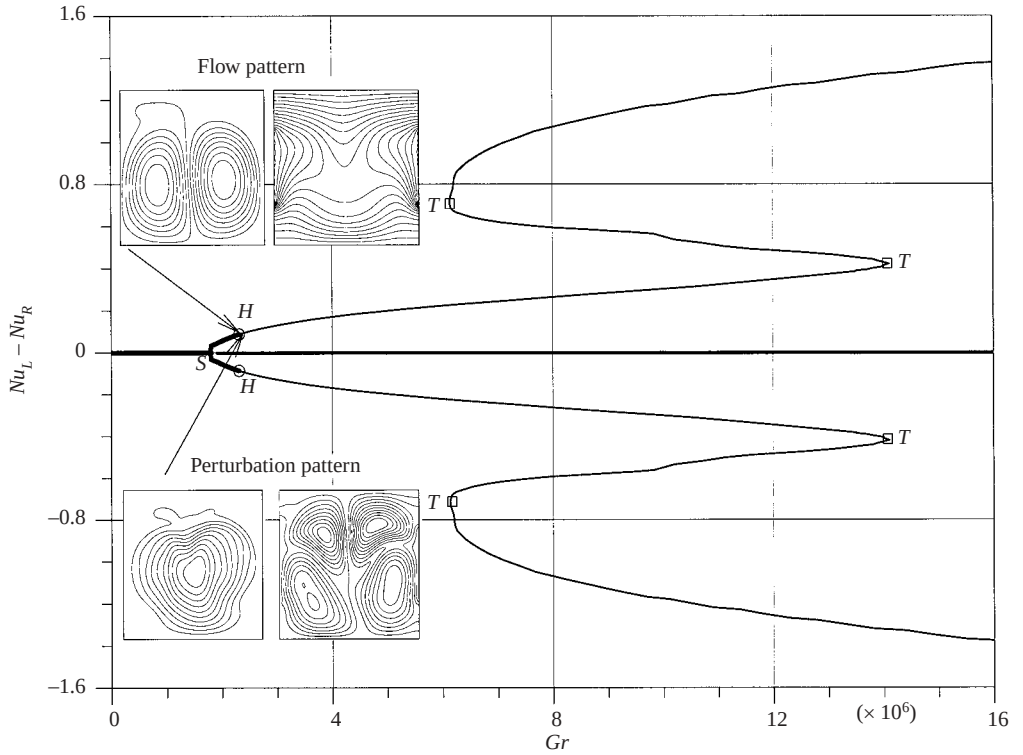

FIGURE 5. Bifurcation diagram for $A = 1.0$. Stable steady states are shown by bold lines. S, point of symmetry-breaking steady bifurcation; T, turning point; H, point of Hopf bifurcation.

most dangerous perturbation leading to the Hopf bifurcation are shown in figure 5 as inserts. The flow consists of two non-symmetric vortices, which are slightly deformed compared with the symmetric case. At relatively large Grashof number, the maximum and minimum of the streamfunction are shifted downwards (see insert in figure 5), which is a result of strong convective motion. Note, that without any flow at $Gr = 0$ the isotherms are symmetric with respect to the horizontal centreline. A closer view on the isotherms of the developed flow shows that the convective circulation drives the hotter fluid from the heated part of the sidewall upwards and along the upper boundary towards the axis, making smaller the horizontal temperature difference near the upper end of the heated sidewall region. The colder fluid is driven by the convective circulation from the axis along the bottom towards the heated part of the sidewall. As a result, the horizontal temperature difference near the lower end of the heated region increases, which intensifies the flow there. Therefore, the flow in the lower part of the cavity becomes stronger than in the upper part. This shift of the circulation downwards takes place for all cavities, but is most pronounced at low aspect ratios ($A = 1$ for figure 5).

The steady non-symmetric flow at $A = 1$ becomes oscillatory-unstable at $Gr = 2.32 \times 10^6$ (points H in figure 5). These two transitions are shown in the stability diagram (figure 4) and only these are experimentally observable by a graduated increase of the Grashof number. The perturbation corresponding to this Hopf bifurcation is distributed over the whole flow region (see insert in figure 5) and causes the oscillations of the vortices, so that the increasing of one of them is

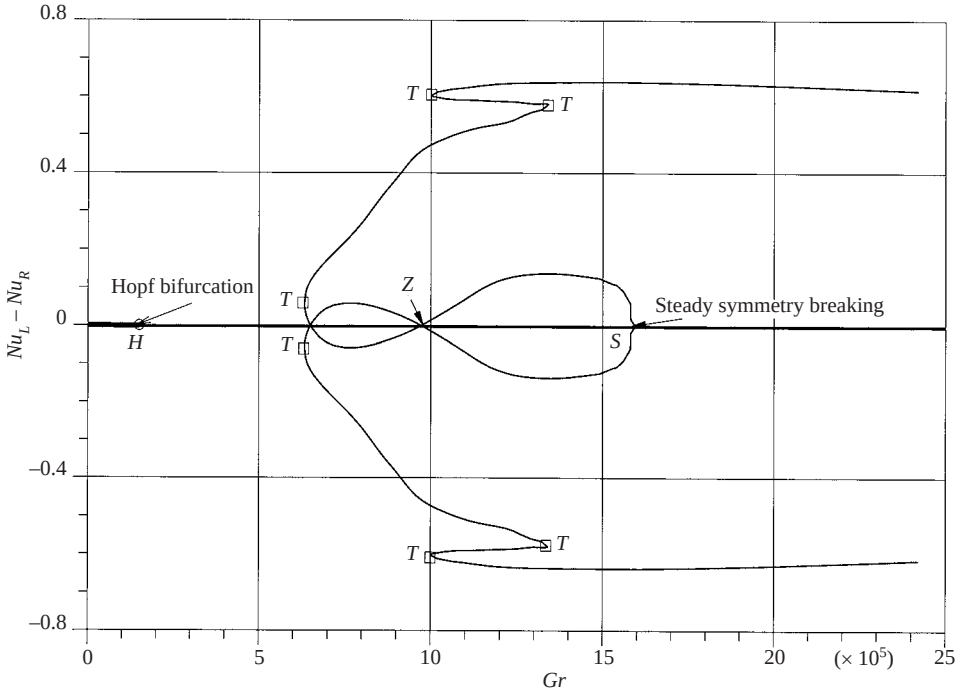

FIGURE 6. As figure 5 for $A = 1.5$.

followed by a decreasing of another one and vice versa. Note, that the calculation of non-symmetric steady states at larger Grashof numbers (beyond points H) reveals two additional turning points at each non-symmetric branch (figure 5), such that between the turning points (denoted as T) in the interval $6.13 \times 10^6 < Gr < 1.41 \times 10^7$ the computational modelling yields seven distinct steady-state solutions. All these solutions are oscillatory-unstable.

In the interval $1.015 \leqslant A \leqslant 2.4$, the symmetric steady states become oscillatory-unstable without undergoing a symmetry-breaking steady bifurcation. However, an increase of the Grashof number beyond the dash–dot curve in figure 4 reveals a complicated behaviour of the two (unstable) non-symmetric steady-state branches. This is shown in figure 6 for $A = 1.5$. Here the steady symmetry-breaking bifurcation (point S) is found far beyond the threshold to the oscillatory state (point H). The two oscillatory-unstable non-symmetric branches, starting at the point S, contain three turning points (points T) each. Note, that the non-symmetric steady states exhibit a hysteretic behaviour, i.e. the non-symmetric solutions exist below the steady symmetry-breaking bifurcation value of Gr (point S).

The behaviour of non-symmetric steady states becomes even more complicated at $A = 2$ (figure 7). Here, the symmetry-breaking Hopf bifurcations occurs at $Gr = 1.42 \times 10^5$ (figure 7*a*, point H). The symmetric flow pattern and the corresponding most dangerous perturbation are shown as inserts. The streamlines pattern is antisymmetric (vortices rotate in the opposite direction) and the isotherms are symmetric with respect to the plane $x = 0.5$. Patterns of the perturbations have the opposite symmetry: the perturbation of the streamfunction is symmetric, while the perturbation of the temperature is antisymmetric. Hence, the resulting oscillatory flow, which is a superposition of the steady state and the oscillating perturbation (multiplied

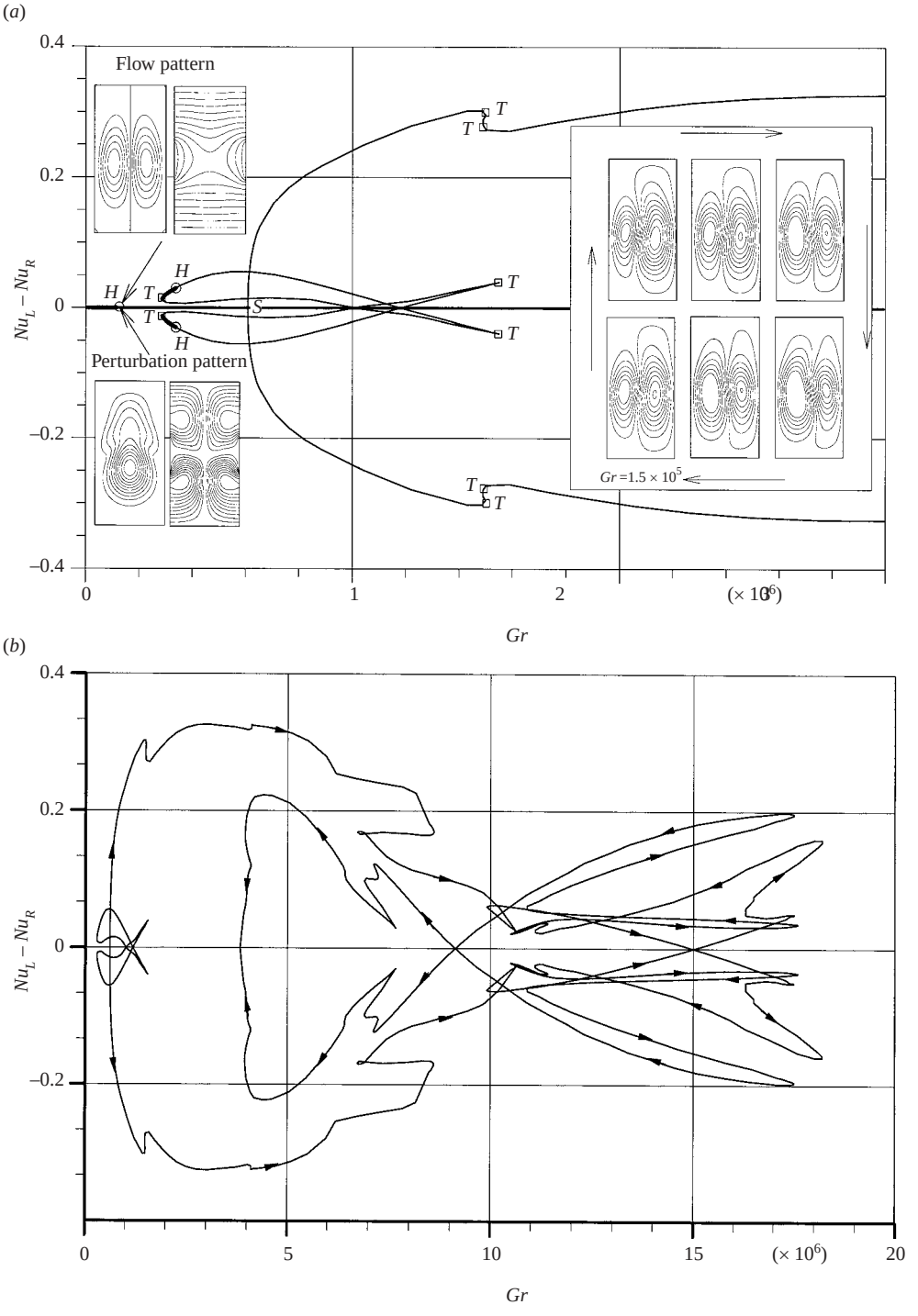

FIGURE 7. As figure 5 for $A = 2.0$. (*a*) A fragment of the diagram corresponding to $Gr = 3 \times 10^6$, (*b*) complete bifurcation diagram.

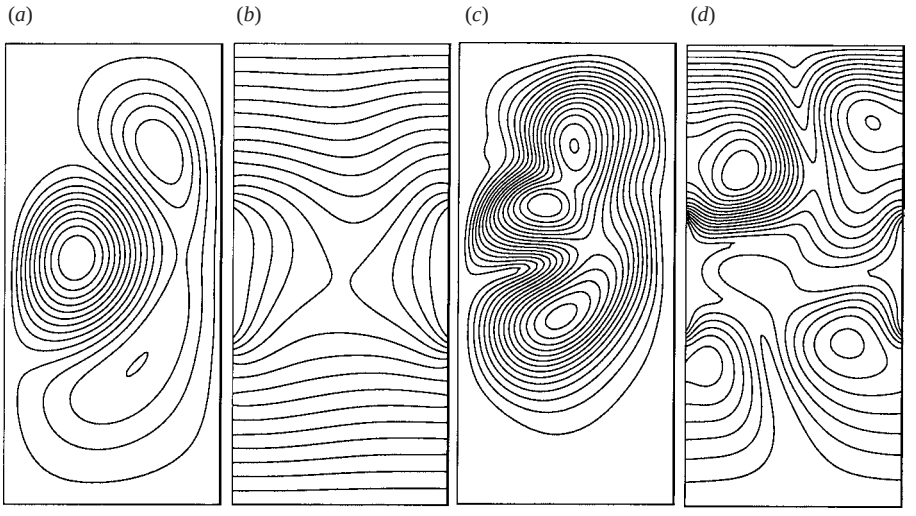

FIGURE 8. Flow and perturbation patterns. Hopf bifurcation of a separated branch of the stable non-symmetric steady state. $A = 2$, $Gr_{cr} = 3.38 \times 10^5$. (*a*) Streamlines, (*b*) isotherms, (*c*) perturbation of stream function, (*d*) perturbation of temperature.

by an amplitude to be computed) is non-symmetric. The weakly nonlinear analysis of Hopf bifurcation (Gelfgat *et al.* 1996; Gelfgat 2001) shows that the bifurcation is supercritical. The snapshots of asymptotic approximation of slightly supercritical oscillatory flow at $Gr = 1.5 \times 10^5$, which corresponds to the supercriticality of 0.67%, are also shown as inserts. The oscillations occur as periodic increase and decrease of each vortex, so that the flow pattern remains non-symmetric during the whole period of the oscillations except two moments of time when both vortices become antisymmetric. Similar oscillations were calculated by Selver *et al.* (1998) by a straightforward integration of the unsteady Navier–Stokes and energy equations. Such symmetry-breaking Hopf bifurcations are observed here in the interval $1.015 < A < 2.4$ (figure 4).

The symmetry-breaking steady bifurcation at $Gr = 6.08 \times 10^5$ (figure 7*a*, point *S*) is found beyond the primary Hopf bifurcation. Besides this, we have found two separated branches of partially stable non-symmetric states (figure 7*a*), which are closed and disconnected from all other branches found. These branches originate from the hysteretic loops shown in figure 6 in the following way. With the increase of aspect ratio the critical Grashof number of the symmetry-breaking steady bifurcation decreases (figure 4), so that the point *S* on the bifurcation diagram (figure 6) moves to the left. When it coincides with the point where $Nu_L - Nu_R = 0$ (point *Z* in figure 6) at the non-symmetric branch, this branch detaches from other solution branches. Note, that in this case (figure 7*a*), in the interval $2.87 \times 10^5 \leqslant Gr \leqslant 6.08 \times 10^5$, there exist four non-symmetric steady states together with one non-symmetric stable oscillatory state. Beyond the symmetry-breaking point *S* in figure 7(*a*), there exist six non-symmetric steady states. Note also that in this interval, $2.87 \times 10^5 \leqslant Gr \leqslant 3.38 \times 10^5$, there exist two stable separated steady states (shown by bold lines) together with the oscillatory non-symmetric state branching from the symmetric steady state at the point *H*. The existence of these stable steady states cannot be predicted by a stability analysis of the initially symmetric steady states. The flow and perturbation patterns of this separated solution are shown in figure 8. Note that the streamline

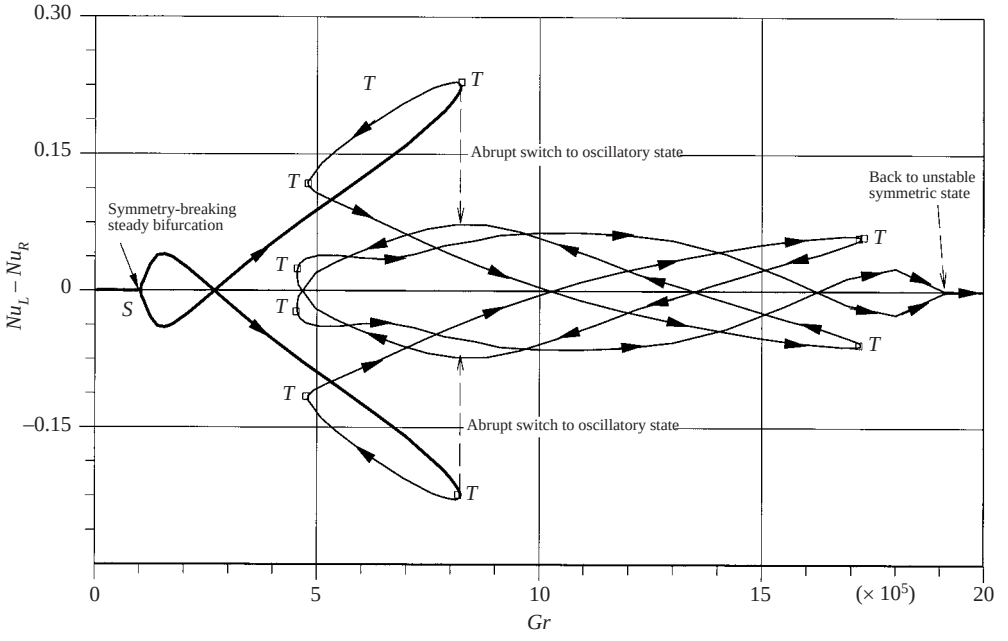

FIGURE 9. As figure 5 for $A = 2.8$.

pattern is strongly deformed compared to the symmetric flow (insert in figure 7*a*), while the non-symmetric shape of the isotherms is not as pronounced. Consequently, the pattern of the streamfunction perturbation differs from that of the symmetric flow (insert in figure 7*a*). At the same time, the pattern of temperature perturbation, affected by the non-symmetric velocity, as well as by non-symmetric perturbation of velocity, is also strongly non-symmetric. The Hopf bifurcation in this case is found to be subcritical. The weakly nonlinear approximation of the supercritical state yields an unstable limit cycle, which is physically unreachable and, therefore, is not illustrated.

Following the development of the steady non-symmetric branches at larger Grashof number a very complicated behaviour was revealed. This is illustrated in figure 7(*b*), where the directions of the path-following are shown by arrows. An unexpected result is the observed merging of the two non-symmetric branches, so that no non-symmetric steady solutions were found beyond $Gr = 1.82 \times 10^7$.

For aspect ratios larger than $A = 2.2$, the non-symmetric steady perturbation becomes the most dangerous and the steady symmetric flow undergoes the symmetry-breaking steady bifurcation, reaching a stable non-symmetric state. The stability properties of the appearing non-symmetric steady flows together with the corresponding bifurcation diagrams change drastically with further increase of the aspect ratio. The bifurcations diagrams exhibit a strong dependence on the aspect ratio, so that it is not possible to illustrate all this richness in the framework of a single paper. We show here only one example for $A = 2.8$ (figure 9).

At $A = 2.8$, the first non-symmetric branch (figure 9) emerges at $Gr = 1.03 \times 10^5$ (point *S*) and remains stable up to the first turning point at $Gr = 8.22 \times 10^5$. Then, it abruptly switches to another oscillatory-unstable non-symmetric branch. Further behaviour of the unstable non-symmetric branch is complicated. The direction of the path-following along the corresponding curves is shown by arrows in figure 9. Note,

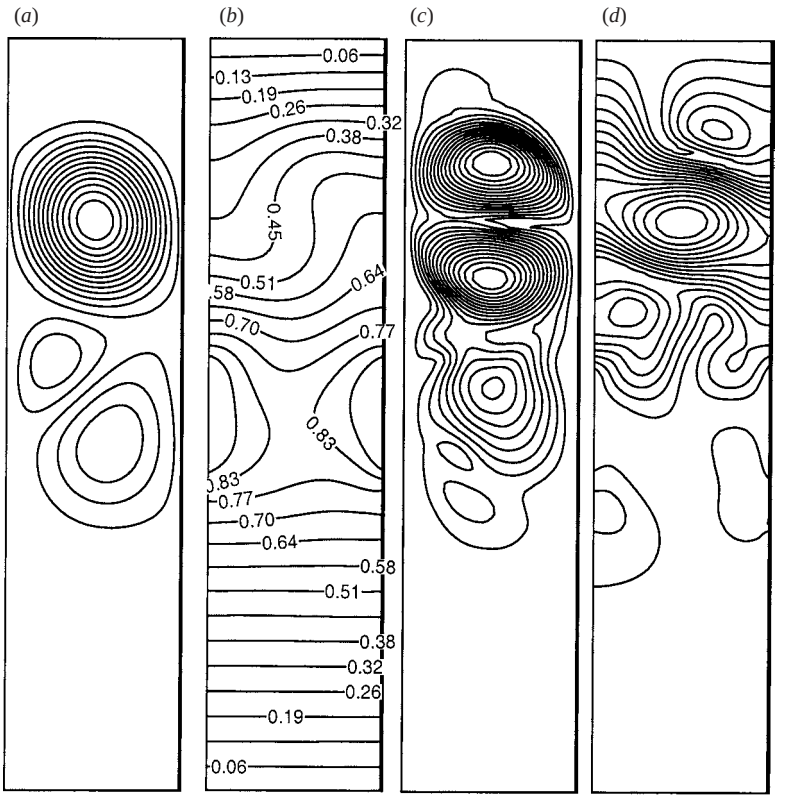

FIGURE 10. Flow and perturbation patterns. Hopf bifurcation of a stable non-symmetric steady state. $A = 4$, $Gr_{cr} = 5.51 \times 10^5$. (*a*) Streamlines, (*b*) isotherms, (*c*) perturbation of stream function, (*d*) perturbation of temperature.

that at $Gr = 1.96 \times 10^6$ both non-symmetric branches merge and only the symmetric unstable branch persists.

In tall cavities, starting from $A \approx 3.1$, the steady instability of an initially symmetric state (like that shown in figure 2*a*) leads to the flow patterns shown in figures 10 and 11 for $A = 4$ and 6, respectively. Here, the most intensive vortex is shifted towards the upper boundary, where the isotherms form an unstably stratified fluid layer. The latter is formed by the hot fluid located near the heated parts of the vertical boundaries and the cold fluid adjacent to the upper boundary. When the characteristic temperature difference inside the layer reaches a critical value, the Rayleigh–Bénard instability mechanism sets in. At the same time, the stably stratified layer (hot fluid above and cold fluid below) is formed in the lower part of the cavity. This stable stratification damps the primary vortices located between the heated parts of the vertical boundaries, so that the most intensive flow is localized in the Rayleigh–Bénard roll. The latter is located in the upper part of the cavity, quite distant from the heated part of the boundaries (see figures 10 and 11). To illustrate the stable and unstable stratifications, the isotherms are labelled. Note that a similar transition driven by the Rayleigh–Bénard mechanism, localized in the upper unstably stratified fluid layer, was observed by Schöpf & Stiller (1997) in a transient convective flow. The Rayleigh–Bénard roll developing in the problem considered is asymptotically stable (i.e. no transient) and therefore exists for an indefinitely long time.

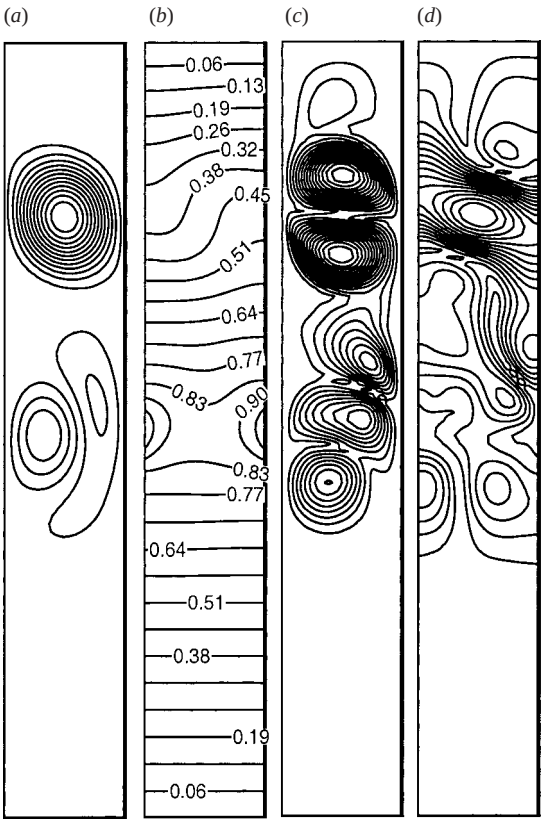

FIGURE 11. Flow and perturbation patterns. Hopf bifurcation of a stable non-symmetric steady state. $A = 6$, $Gr_{cr} = 4.69 \times 10^5$. (*a*) Streamlines, (*b*) isotherms, (*c*) perturbation of stream function, (*d*) perturbation of temperature.

As can be seen from figures 10 and 11, the combined effect of the Rayleigh–Bénard instability mechanism and the damping effect caused by the stable stratification leads to a complete change of the flow pattern. The primary vortex located in the upper part of the cavity is driven by the Rayleigh–Bénard mechanism, while the secondary vortices below it are driven by the buoyancy force, which is large near the heated parts of the boundaries. The secondary vortices are damped inside the stably stratified part of the fluid. A similar change of the flow pattern, caused by the Rayleigh–Bénard instability mechanism, was observed in cylindrical containers (Gelfgat *et al.* 1999*b*, 2000). There, the steady axisymmetry-breaking instability, caused by the Rayleigh–Bénard instability mechanism, was also observed inside the unstably stratified layers that form under certain heating conditions. An example in § 4.4 shows that this mechanism persists also in cylinders with a partially heated sidewall.

Patterns of the most dangerous perturbations corresponding to the Hopf bifurcations of non-symmetric steady flow in tall cavities (figures 10 and 11) show that the oscillatory instability also sets in inside the unstably stratified layers, i.e. in the upper parts of the cavities. In taller cavities (figure 11) the perturbation of the streamfunction propagates downwards causing oscillations of the secondary vortices together with the primary Rayleigh–Bénard vortex.

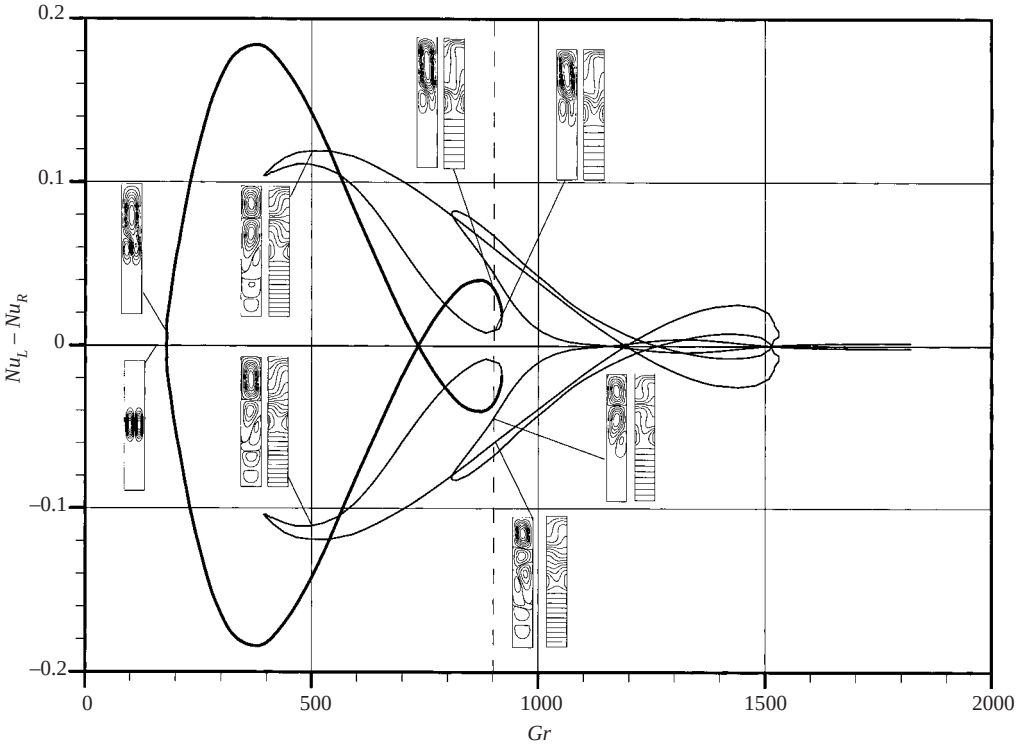

FIGURE 12. Bifurcation diagram for $Pr = 10$, $A = 6$.

To illustrate that the described Rayleigh–Bénard mechanism leads to a similar change in the flow pattern at larger Prandtl numbers, the bifurcation diagram for $Pr = 10$ and $A = 6$, is shown in figure 12. Here, the steady symmetry-breaking bifurcation takes place at $Gr = 179$ and the non-symmetric steady flow remains stable up to the first turning point at $Gr = 919$. This is similar to the bifurcation diagram shown in figure 9. As above, the curves corresponding to stable flows are shown by thicker lines. Several inserts in figure 12 illustrate the changes in the flow pattern with increasing Grashof number. The flow patterns are shown in the vicinity of the symmetry-breaking bifurcation point and in the cross-sections $Gr = 500$ and 900. Note, that most of the non-symmetric flow patterns corresponding to $Gr \geqslant 500$ can be characterized by a localization of the strongest vortex in the upper part of the cavity and the weakened motion near the heated parts of the sidewalls. These flow structures develop owing to the Rayleigh–Bénard mechanism described above for the low-Prandtl-number fluid case. The effect of the Prandtl number is clearly seen by comparison of the flow patterns at $Pr = 0.021$ and 10. At larger Pr, the convective mixing is stronger which leads to a faster motion along the boundaries and weakens the motion in the bulk of the flow.

4.4. *Three-dimensional instability of the axisymmetric flow in a cylinder: an example*

To model the experimental configuration of Selver *et al.* (1998), we have to reformulate the problem as convection in a vertical cylinder with a partially heated sidewall. Thus, for the problem sketched in figure 1 the Cartesian coordinates x and y must be replaced by cylindrical coordinates r and z, and the plane of symmetry by the polar symmetry axis. Consequently, the equations and the boundary conditions must be

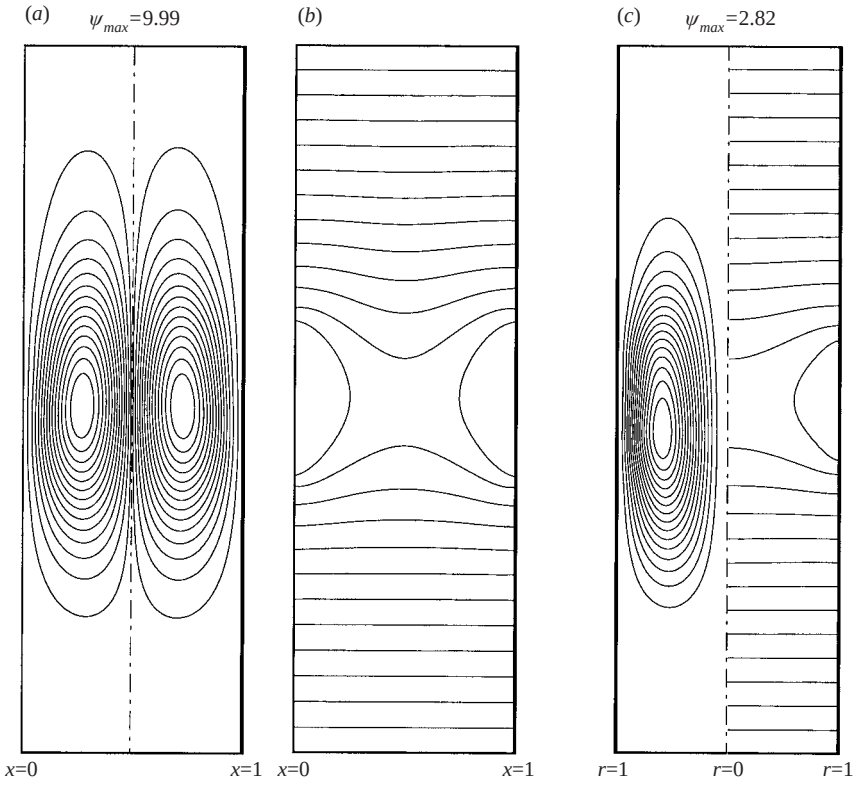

FIGURE 13. (*a*) Streamlines and (*b*) isotherms of the flow in a two-dimensional cavity ($Gr_{cr} = 9.6 \times 10^4$) and (*c*) those in a vertical cylinder ($Gr_{cr} = 1.5 \times 10^5$) with a partially heated sidewall. A = height/length = height/diameter = 3.

reformulated. The details on implementation of the global Galerkin method for three-dimensional flows in cylindrical coordinates can be found in Gelfgat *et al.* (1999*b*) and Gelfgat (2001).

Our primary interest is the stability of the base axisymmetric flow with respect to all possible infinitesimal three-dimensional perturbations. The perturbations are represented as Fourier harmonics in the azimuthal direction, whose amplitudes are dependent on the meridional variables in the directions r and z, i.e. a perturbation has the form $P_k(r, z)\exp(\mathrm{i}k\theta)$, where k is an integer. It is well known that the linear stability problem separates for each value of k, so that a solution of a sequence of linearized stability problems for different values of k allows us to investigate the three-dimensional instability of an axisymmetric flow.

Note that the axisymmetric mode $k = 0$ is analogous to the plane case in which the non-symmetric perturbations are excluded (dotted curve in figure 4). Similarly to the plane case, the marginal Grashof number corresponding to the onset of the axisymmetric mode ($k = 0$) is far above the marginal numbers for the three-dimensional modes $k \neq 0$. For the problem described, our preliminary computations show that, depending on the cylinder aspect ratio, the primary instability sets in for $k = 1$ or 2. Note that the three-dimensional modes with $k = 1$ represent a 2π–periodic deformation of the axisymmetric toroidal vortex, which leads to a non-symmetric flow pattern in any diametral cross-section (a cross-section by a plane containing the polar axis) of the cylinder. Thus, the $k = 1$ mode can be associated with non-symmetric plane

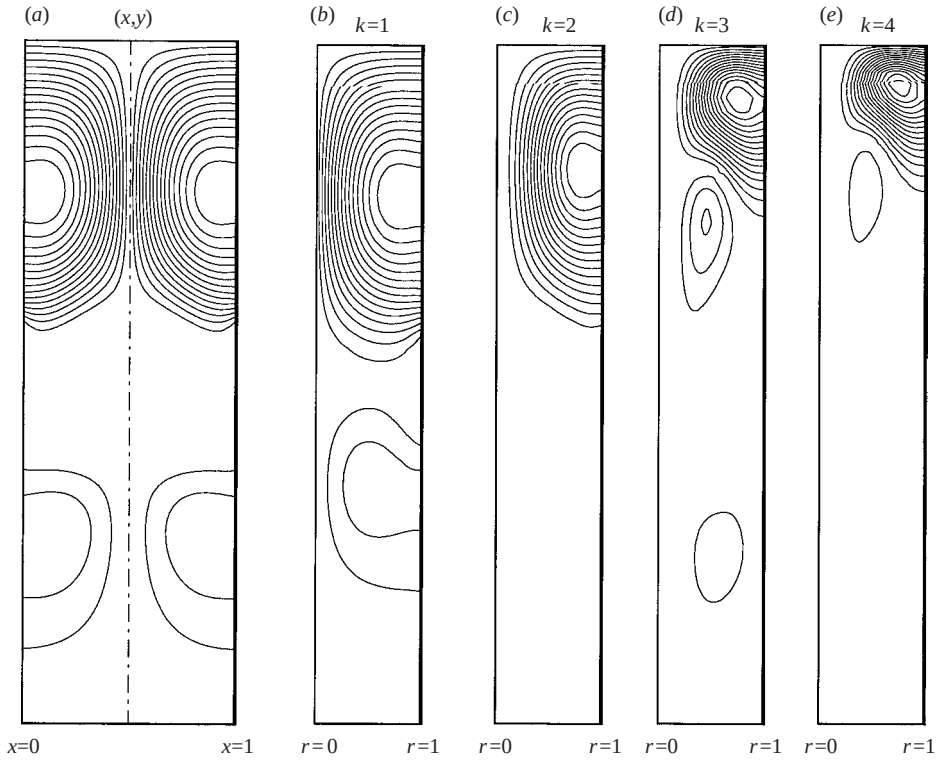

FIGURE 14. (*a*) Amplitude of the temperature perturbations for symmetry-breaking bifurcation in the two-dimensional cavity and (*b–e*) the four most dangerous modes of the three-dimensional perturbations of the flow in a cylinder shown in figure 13.

modes. The modes with $k > 1$ represent the appearance of $2\pi/k$–azimuthally periodic three-dimensional structures, which are ordered around the axis. These modes can be regarded as analogous to with the three-dimensional transverse perturbations in the Cartesian coordinates, which were not considered in the previous analysis.

In the following example, we focus on the flow in a cylinder with aspect ratio ($A_D =$ height/diameter) 3 and compare it with the plane case of the same value of the aspect ratio $A = 3$. All other parameters are defined as for the problem considered above. The axisymmetric base flow is compared with the corresponding flow in the two-dimensional cavity in figure 13. Both flow patterns are shown for the critical Grashof numbers corresponding to the symmetry-breaking bifurcations, which are the breaking of the reflection symmetry for the flow in the plane cavity and the axisymmetry–three-dimensional transition via the mode $k = 1$ for the flow in the cylinder. Note that the flow in the plane cavity is significantly more intensive in spite of the lower critical Grashof number. However, the temperature fields are similar in both cavities, which means that in both cases there was established a similar equilibrium between conductive and convective heat transfer.

As mentioned above, the instability in tall cavities sets in owing to the Rayleigh–Bénard instability in the unstably stratified layer located in the upper part of the cavity. The depths of the unstably stratified layers are almost equal in both the Cartesian and cylindrical cases (figure 13), so we expect to see similar perturbation patterns. The latter is illustrated in figure 14, where the isolines of the amplitudes $P_k(r, z)$ of the

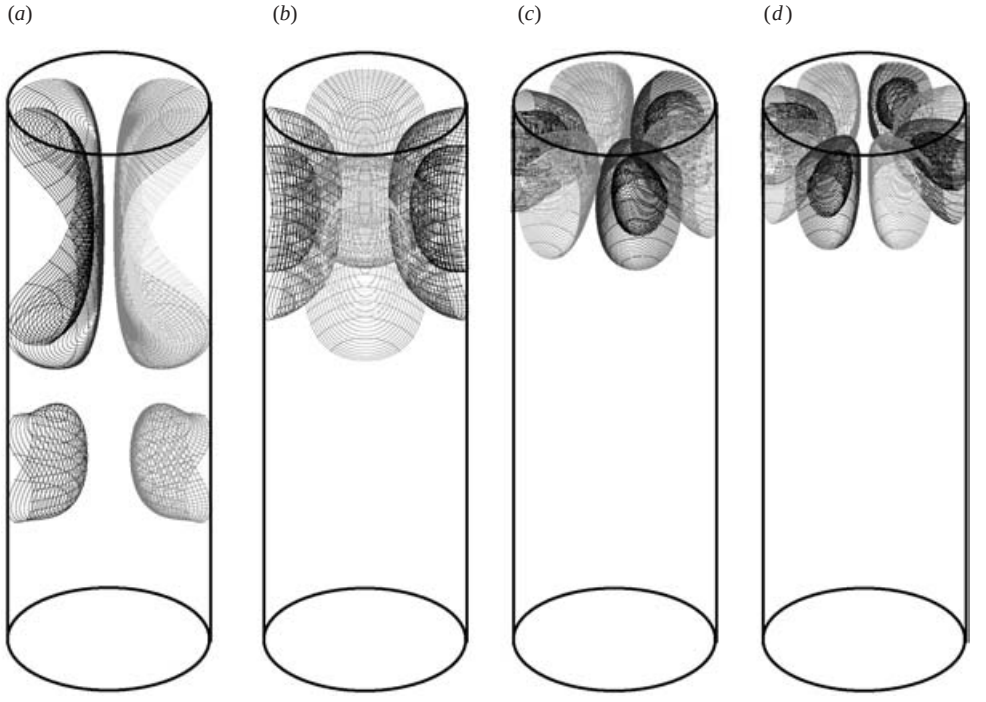

FIGURE 15. Patterns of the three-dimensional perturbations of the temperature for the three-dimensional stability analysis of the flow shown in figure 14. (*a*) $k=1$, (*b*) $k=2$, (*c*) $k=3$, (*d*) $k=4$.

three-dimensional perturbation of the temperature for $k=1, 2, 3$ and 4 are compared with the temperature perturbation in the plane cavity. The corresponding marginal values of the Grashof number are 1.5×10^5, 6.8×10^5, 1.2×10^6, and 2.7×10^6 for $k=1, 2, 3$ and 4, respectively. All four modes are stationary, i.e. the imaginary parts of the associated leading eigenvalues are zero. The most dangerous perturbation mode is the mode with $k=1$, which, as expected, has a pattern similar to that of the plane symmetry-breaking perturbation. Moreover, the experimental observations of Selver *et al.* (1998), made for the cylinder aspect ratios 4, 8 and 12, showed that the supercritical three-dimensional pattern has the circumferential periodicity corresponding to the Fourier mode $k=1$ in our description. This agrees qualitatively with the present results.

Note that the most dangerous perturbation tends to occupy the whole unstably stratified volume (figure 14). The modes with larger azimuthal wavenumbers ($k>1$) occupy smaller volumes, since they correspond to a larger number of Rayleigh–Bénard rolls, which must be packed around the axis. This can be seen in the three-dimensional patterns of the temperature perturbation shown in figure 15. Each pair of neighbouring structures in figure 15 corresponds to one Rayleigh–Bénard roll, so that the fluid ascends where the perturbation has a maximum (darker isosurfaces) and descends where the perturbation has a minimum (lighter isosurfaces). Obviously, the absolute amplitudes of the perturbations are not defined by the linear stability analysis, thus the isosurfaces are not labelled. Owing to the axisymmetric boundary conditions, the azimuthal location of the rolls is arbitrary.

The modes corresponding to $k > 1$ can be associated with the longitudinal rolls, which can be expected for the two-dimensional flow if all three-dimensional infinitesimal perturbations are considered. It was shown by Gelfgat (1999) that the most dangerous perturbation in a three-dimensional rectangular box can be either longitudinal or transverse rolls, where the result depends strongly on the extent of the container in the third dimension (the width ratio). As mentioned, the appearance of the longitudinal rolls in the problem considered can only add to the multiplicity of flow states, and therefore will not change the qualitative conclusions drawn above. We prefer, however, to consider the three-dimensional stability problem for the cylindrical cavity, which (i) corresponds to the experiment and (ii) does not increase the number of characteristic parameters.

Besides the Rayleigh–Bénard modes illustrated in figures 14 and 15, we observed also the oscillatory modes with $k = 1$ and 2, which are characteristic for cylinders of smaller aspect ratio, $1 < A < 3$. These modes also have certain similarities with the oscillatory modes reported here for the rectangular cavity and can be associated with the hydrodynamic instability of the flow. Since all the instabilities reported for the rectangular cavity are present also in the cylindrical one, we expect a multiplicity of the supercritical three-dimensional states, similar to the multiplicity observed in the rectangular cavities. However, application of the path-continuation techniques to the three-dimensional states is yet to be developed and is beyond the scope of the present study.

5. Conclusions and discussion

The multiplicity and stability of steady convective flows in two-dimensional rectangular cavities with partially and symmetrically heated vertical walls were studied computationally. The stability diagram shows the marginal stability curves corresponding to the steady symmetry breaking and Hopf bifurcations. It is shown that a solution of the problem in a half-cavity, assuming symmetry, leads to wrong conclusions regarding the stability of primary flows and misses all possible non-symmetric solutions.

The main and the most unexpected result of the present study is the existence of multiple supercritical steady flows, which appear as a result of folding via a series of turning-point bifurcations of the non-symmetric solution branches, as well as their possible detachment from the main branches. Although most of the multiple steady flows are unstable, there exist also stable steady states separated from main stable solution branches. On the basis of the results obtained for the multiplicity of steady flows, it is expected that laminar oscillatory flows exist around each unstable steady-state branch. This leads to a multiplicity of steady and oscillatory states. It is emphasized that at sufficiently large Grashof numbers (however, far below the threshold to turbulence), the final asymptotic state of these flows is strongly dependent on particular initial conditions and computational (experimental) path. Where different initial conditions yield different asymptotic states numerically, we would expect to observe also the corresponding different flow patterns experimentally.

Patterns of the multiple steady-state flows reveal three competing mechanisms, responsible for the observed complicated changes of the flow structure. The first and the most obvious one is the buoyant convection driven by the heated parts of the vertical boundaries. This mechanism creates completely symmetric primary flow patterns. The symmetry can be broken via a symmetry-breaking steady pitchfork bifurcation, which is caused by a pure hydrodynamic instability mechanism (i.e.

such bifurcation can be found also for $Pr = 0$, i.e. when the convection of heat is neglected). The second is the Rayleigh–Bénard instability, which develops in the upper part of the cavity containing the unstably stratified fluid. This mechanism turns out to be dominant after the temperature gradient inside the unstably stratified fluid exceeds a certain critical value, and is characteristic for tall cavities and relatively large Grashof numbers. The third mechanism is connected with the existence of the stable stratification in the lower part of the cavity and causes the damping of any fluid motion in that region. It is concluded that the combined action of these three mechanisms causes the observed multiplicity of steady (and possibly, oscillatory) flows.

It is emphasized that the flow patterns that develop in containers with partially heated sidewalls differ qualitatively from those developing in the case of uniformly heated boundaries. The cellular flow patterns developing in horizontal (Cross *et al.* 1983; Drummond & Korpela 1987; Gelfgat 1999; Gelfgat *et al.* 1999*a*) and vertical (Lee & Korpela 1983; Lartigue, Lorents & Bourret 2000) finite cavities with uniformly heated horizontal or vertical boundaries can be characterized by convective cells distributed almost uniformly along one of the boundaries (usually, the longest boundary). In cases of side heating, most of the flow energy belongs to the main circulation, not to the cells. In the case considered, we observed a transition from a convective flow located near the heated elements, as was expected, to an unexpected pattern characterized by a vortex located in the upper part of the cavity far from the heated region. Applying a certain idealization we can explain this observation as follows: the heat is transferred from a heated element to the upper part of the cavity mainly by conduction, where it triggers the Rayleigh–Bénard convective mechanism. The developing single Rayleigh–Bénard vortex absorbs most of the flow energy.

It is shown that there exists a similarity between the onset of instability in the two-dimensional cavity and a three-dimensional instability of the axisymmetric flow in a vertical cylinder. The present results predicting the multiplicity of steady and oscillatory flow states in rectangular cavities allow us to foresee a similar multiplicity of supercritical three-dimensional flows in cylinders, which has to be expected after the initial axial symmetry is broken by a primary instability. Apparently, the observed flow and instability driving mechanisms are common for tall cavities with a localized heating of the sidewalls. Therefore, the phenomenon observed should be expected in most buoyancy-driven flows caused by such a localized heating.

The large number of multiple solutions in the present model flow is exceptional. However, the multiplicity of steady and oscillatory flow states was observed in other studies dealing with confined convective and rotating flows (see, for example, Coles 1965; Cross *et al.* 1983; Cliffe & Mullin 1985; Schrauf 1986; Bar-Yoseph 1994; Gelfgat 1999; Gelfgat *et al.* 1999*a*; Pallares *et al.* 1999; Lopez, Marques & Sanchez 2001). Therefore, it can be concluded that the multiplicity of laminar flow states at relatively large values of the characteristic parameters (e.g. Reynolds, Grashof and Taylor numbers) is quite a common property, which should be accounted for.

The computation of multiple solutions and the analysis of their stability require an extension of the usual computational approaches. In particular, direct solvers for steady-state flows, path-continuation techniques and eigenvalue solvers should be used along with the traditional time-marching approaches. Thus, the previous time-dependent computations for the present problem performed by Selver *et al.* (1998) identified only two out of the eleven possible solutions, which are presented here. In particular, the non-symmetric flow state found by Selver *et al.* (1998) agrees very well with the critical Grashof number $Gr_{cr} = 9.0 \times 10^4$, computed in the present study. The

other nine possible states, however, could not be found by a straightforward time integration without the corresponding changes in the initial conditions. As a rule, the initial conditions that are attracted to a certain solution branch are unknown. The computational path-continuation techniques, like the one used here, allow us to follow these branches and to generate the corresponding initial conditions, if necessary. The experiments conducted by Selver *et al.* (1998) in a cylindrical geometry exhibited axisymmetry-breaking bifurcations, which can be associated with the symmetry-breaking bifurcations in rectangular cavities described here. Note, that the flow in a cylindrical container with a partially heated cylindrical wall is subjected to the same instability mechanisms as its rectangular counterpart. Therefore, we can expect a multiplicity of supercritical three-dimensional flows appearing beyond the axisymmetry breaking bifurcations in the cylindrical container.

Finally, it is noticed that the simple physical model considered exhibits a variety of steady, turning-point and Hopf bifurcations. This makes it attractive as a challenging benchmark problem for numerical methods dealing with the path continuation and stability analysis (Henry & Dijkstra 2000).

This work was supported by the Israel Ministry of Science (Grant 8575-1-98), the Israel Science Foundation (Grant 240/01), The Center for Absorption in Science, Israel Ministry of Immigrant Absorption (to V. E. and A. Yu. G.), the Fund for the Promotion of Research at the Technion, the Israel High Performance Computer Unit, and the Y. Winograd Chair of Fluid Dynamics and Heat Transfer at the Technion.

REFERENCES

Bar-Yoseph, P. 1994 On multiple flow patterns and vortex breakdown phenomena in confined rotating flows. *Comput. Fluid Dyn. J.* **3**, 273–292.

Bergholz, R. F. 1978 Instability of steady natural convection in a vertical fluid layer. *J. Fluid Mech.* **84**, 743–768.

Busse, F. H. 1967 The stability of finite amplitude cellular convection and its relation to an extremum principle. *J. Fluid Mech.* **30**, 625–649.

Chadwick, M. L., Webb, B. W. & Heaton, H. S. 1991 Natural convection from two-dimensional discrete heat sources in a rectangular enclosure. *Intl J. Heat Mass Transfer* **34**, 1679–1693.

Cliffe, K. A. & Mullin, T. 1985 A numerical and experimental study of anomalous modes in the Taylor experiment. *J. Fluid Mech.* **153**, 243–258.

Coles, D. 1965 Transition in circular Couette flow. *J. Fluid Mech.* **21**, 385–425.

Cross, M. C., Daniels, P. G., Hohenberg, P. C. & Siggia, E. D. 1983 Phase-winding solutions in a finite container above the convective threshold. *J. Fluid Mech.* **127**, 155–183.

Drummond, J. E. & Korpela, S. A. 1987 Natural convection in a shallow cavity. *J. Fluid Mech.* **182**, 543–564.

Frederick, R. L. & Quiroz, F. 2001 On the transition from conduction to convection regime in a cubical enclosure with a partially heated wall. *Intl J. Heat Mass Transfer* **44**, 1699–1709.

Fu, W.-S., Tseng, C.-C. & Chen, Y.-C. 1994 Natural convection in an enclosure with non-uniform wall temperature. *Intl J. Heat Mass Transfer* **21**, 819–828.

Gelfgat, A. Yu. 1999 Different modes of Rayleigh–Bénard instability in two- and three-dimensional rectangular enclosures. *J. Comput. Phys.* **156**, 300–324.

Gelfgat, A. Yu. 2001 Two- and three-dimensional instabilities of confined flows: numerical study by a global Galerkin method. *Comput. Fluid Dyn. J.* **9**, 437–448.

Gelfgat, A., Bar-Yoseph, P. Z. & Solan, A. 1996 Stability of confined swirling flow with and without vortex breakdown. *J. Fluid Mech.* **311**, 1–36.

Gelfgat, A. Yu., Bar-Yoseph, P. Z. & Solan, A. 2000 Axisymmetry breaking instabilities of natural convection in a vertical Bridgman growth configurations. *J. Cryst. Growth* **220**, 316–325.

Gelfgat, A. Yu., Bar-Yoseph, P. Z., Solan, A. & Kowalewski, T. 1999*b* An axisymmetry-breaking instability in axially symmetric natural convection. *Intl J. Transport Phenomena* **1**, 173–190.

Gelfgat, A. Yu., Bar-Yoseph, P. Z. & Yarin, A. L. 1997 On oscillatory instability of convective flows at low Prandtl number. *J. Fluids Engng* **119**, 823–830.

Gelfgat, A. Yu., Bar-Yoseph, P. Z. & Yarin, A. L. 1999*a* Stability of multiple steady states of convection in laterally heated cavities. *J. Fluid Mech.* **388**, 315–334.

Gelfgat, A. Yu. & Tanasawa, I. 1994 Numerical analysis of oscillatory instability of buoyancy convection with the Galerkin spectral method. *Numer. Heat Transfer* A **25**, 627–648.

Henry, D. & Dijkstra, H. (ed.) 2000 Continuation methods in fluid dynamics. Contributions to the ERCOFTAC/EUROMECH Colloquium 383, Aussois, France, 6–9 September 1998. *Notes on Numerical Fluid Mechanics*. Vieweg.

Ho, C. J. & Chang, J. Y. 1994 A study of natural convection heat transfer in a vertical rectangular enclosure with two-dimensional discrete heating: effect of aspect ratio. *Intl J. Heat Mass Transfer* **37**, 917–925.

Kamotani, Y., Weng, F.-B., Ostrach, S. & Platt, J. 1994 Oscillatory natural convection of a liquid metal in circular cylinders. *J. Heat Transfer* **116**, 627–632.

Keller, H. B. 1977 Numerical solution of bifurcation and nonlinear eigenvalue problems. In *Applications of Bifurcation Theory* (ed. P. H. Rabinowitz), pp. 359–384. Academic.

Keyhani, M., Prasad, V. & Cox, R. 1988 An experimental study of natural convection in a vertical cavity with discrete heat sources. *J. Heat Transfer* **110**, 616–624.

Khalilollahi, A. & Sammakia, B. 1986 Unsteady natural convection generated by a heated surface within an enclosure. *Numer. Heat Transfer* **9**, 715–730.

Kitamura, K., Komiyama, K. & Saito, T. 1984 Oscillatory motion of natural convection in rectangular cavity. *Bull. JSME* **27**, 2463–2469.

Kuhn, D. & Oosthuizen, P. H. 1987 Unsteady natural convection in a partially heated rectangular cavity. *J. Heat Transfer* **109**, 798–801.

Lakhal, E. K., Hasnaoui, M. & Vasseur, P. 1999 Numerical study of transient natural convection in a cavity heated periodically with different types of excitations. *Intl J. Heat Mass Transfer* **42**, 3927–3941.

Lakhal, E. K., Hasnaoui, M., Vasseur, P. & Bilgen, E. 1994 Natural convection in a square enclosure heated periodically from part of the bottom wall. *Numer. Heat Transfer* A **27**, 319–333.

Lartigue, B., Lorente, S. & Bourret, B. 2000 Multicellular natural convection in a high aspect ratio cavity: experimental and numerical results. *Intl J. Heat Mass Transfer* **43**, 3157–3170.

Lee, Y. & Korpela, S. A. 1983 Multicellular natural convection in a vertical slot. *J. Fluid Mech.* **126**, 91–121.

Lopez, J. M., Marques, F. & Sanchez, J. 2001 Oscillatory modes in an enclosed swirling flow. *J. Fluid Mech.* **439**, 109–129.

Müller, G. & Ostrogorsky, A. 1994. Convection in melt growth. In *Handbook of Crystal Growth* (ed. D. T. J. Hurle), vol. 2, pp. 711–781. North-Holland.

November, M. & Nansteel, M. W. 1987 Natural convection in rectangular enclosure heated from below and cooled along one side. *Intl J. Heat Mass Transfer* **30**, 2433–2440.

Pallares, J., Grau, F. X. & Giralt, F. 1999 Flow transitions in laminar Rayleigh–Bénard convection in a cubical cavity at moderate Rayleigh numbers. *Intl J. Heat Mass Transfer* **42**, 753–769.

Poulikakos, D. 1985 Natural convection in a confined fluid-filled space driven by a single vertical wall with warm and cold regions. *J. Heat Transfer* **107**, 867–876.

Schöpf, W. & Stiller, O. 1997 Three-dimensional patters in a transient, stratified intrusion flow. *Phys. Rev. Lett.* **79**, 4373–4376.

Schrauf, G. 1986. The first instability in spherical Couette–Taylor flow. *J. Fluid Mech.* **166**, 287–303.

Selver, R., Kamotani, Y. & Ostrach, S. 1998 Natural convection of a liquid metal in vertical cylinders heated locally from the side. *J. Heat Transfer* **120**, 108–114.

Sezai, I. & Mohamad, A. A. 2000 Natural convection from a discrete heat source on the bottom of a horizontal enclosure. *Intl J. Heat Mass Transfer* **43**, 2257–2266.

Tsitverblit, N. & Kit, E. 1993 The multiplicity of steady flows in confined double-diffusive convection with lateral heating. *Phys. Fluids* A **5**, 1062–1064.